Molecular-Level Exploration of the Structure-Function Relations Underlying Interfacial Charge Transfer in the Subphthalocyanine/C_{60} Organic Photovoltaic System

Jacob Tinnin,[1,2] Srijana Bhandari,[3] Pengzhi Zhang,[1] Huseyin Aksu,[3] Buddhadev Maiti,[3] Eitan Geva,[4,*] Barry D. Dunietz,[3,†] Xiang Sun,[5,6,7,‡] and Margaret S. Cheung[1,2,§]

[1] *Department of Physics, University of Houston, 617 Science and Research Building 1, Houston, Texas 77204, USA*
[2] *Center for Theoretical Biological Physics, Rice University, 6500 Main Street, BioScience Research Collaborative, Suite 1005G, Houston, Texas 77030-1402, USA*
[3] *Department of Chemistry and Biochemistry, Kent State University, 1175 Risman Drive, Kent, Ohio 44242, USA*
[4] *Department of Chemistry, University of Michigan, 930 North University Avenue, Ann Arbor, Michigan 48109, USA*
[5] *Division of Arts and Sciences, New York University Shanghai, 1555 Century Avenue, Shanghai 200122, China*
[6] *Department of Chemistry, New York University, New York, New York 10003, USA*
[7] *NYU-ECNU Center for Computational Chemistry at New York University Shanghai, 3663 Zhongshan Road North, Shanghai 200062, China*

(Received 4 December 2019; revised manuscript received 22 March 2020; accepted 17 April 2020; published 28 May 2020)

The arrangement of organic molecules at the donor-acceptor interface in an organic photovoltaic (OPV) cell can have a strong effect on the generation of charge carriers and thereby cell performance. In this paper, we report the molecular-level exploration of the ensemble of interfacial donor-acceptor pair geometries and the charge-transfer (CT) rates to which they give rise. Our approach combines molecular-dynamics simulations, electronic structure calculations, machine learning, and rate theory. This approach is applied to the boron subphthalocyanine chloride (donor) and C_{60} (acceptor) OPV system. We find that the interface is dominated by a previously unreported donor-acceptor pair *edge* geometry, which contributes significantly to device performance in a manner that depends on the initial conditions. Quantitative relations between the morphology and CT rates are established, which can be used to advance the design of more efficient OPV devices.

DOI: 10.1103/PhysRevApplied.13.054075

I. INTRODUCTION

Research into organic photovoltaic (OPV) cells is motivated by the synthetic tunability, plasticity, and low manufacturing and environmental costs of the materials in comparison with those used in inorganic photovoltaic (PV) cells [1–6]. Within OPV cells, electron donor molecules are photoexcited by incident light to form localized electron-hole pairs, or excitons. These excitons then diffuse through the donor layer to the donor-acceptor interface, where they undergo donor-to-acceptor charge transfer (CT) [1,2,7], which is the first step toward charge separation and the generation of an electrical current. Thus, improving the performance of OPV cells calls for a better understanding of the ensemble of donor-acceptor (D-A) pair geometries and their correlation with the interfacial CT rates to which they give rise [5,8–11].

In this paper, we investigate the relationships between interfacial structure and CT rates in an OPV cell consisting of boron subphthalocyanine (SubPC) as the electron D and fullerene (C_{60}) as the electron A [1,3,5,12–15]. The SubPC/C_{60} cell continues to draw a wide research effort as a model of OPV systems [14–18].

For example, the SubPC/C_{60} cell parameters have been shown to depend on the fabrication scheme and surface morphology [3,5,19,20]. The goal of this paper is twofold. First, we aim to provide insights on the relationships between interfacial structure and CT kinetics and to develop a comprehensive computational framework that will be implemented to design OPV cells of enhanced efficiencies. We hope that the lessons learned from the study of the model system will inspire new design strategies of OPV cells. Furthermore, the computational framework as reported here is expected to play a role in the search for such enhanced OPV applications.

*eitan@umich.edu
†bdunietz@kent.edu
‡xiang.sun@nyu.edu
§mscheung@uh.edu

Previous computational studies of the correlation between interfacial structure and CT rates in the SubPC/C_{60} system and similar phthalocyanine-fullerene systems have been based on the optimal geometries of D-A pairs embedded in a polarized-continuum model (PCM) [1,13,18,21,22], which can only account for the effect of the solid-state host in a mean-field manner. The earlier SubPC studies identified two key interfacial D-A pair geometries, referred to as *on-top* and *hollow* [see Figs. 1(a) and 1(b), respectively]. It should be noted that C_{60} is a spherical molecule, while SubPC is bowl shaped. The *on-top* geometry corresponds to the case in which the concave side of the SubPC faces the C_{60}, while the *hollow* geometry corresponds to the case in which the convex side of the SubPC faces the C_{60}.

Importantly, a mean-field modeling at the PCM level cannot account for the many-body effects brought about by the nonuniform molecular nature of the solid-state environment [8,23,24]. More specifically, the optimal D-A pair optimal geometries may not be representative of the actual geometries found in a solid-state system. Furthermore, treating the environment as a dielectric continuum cannot account for the fact that there is likely a distribution of geometries, rather than a few well-defined ones.

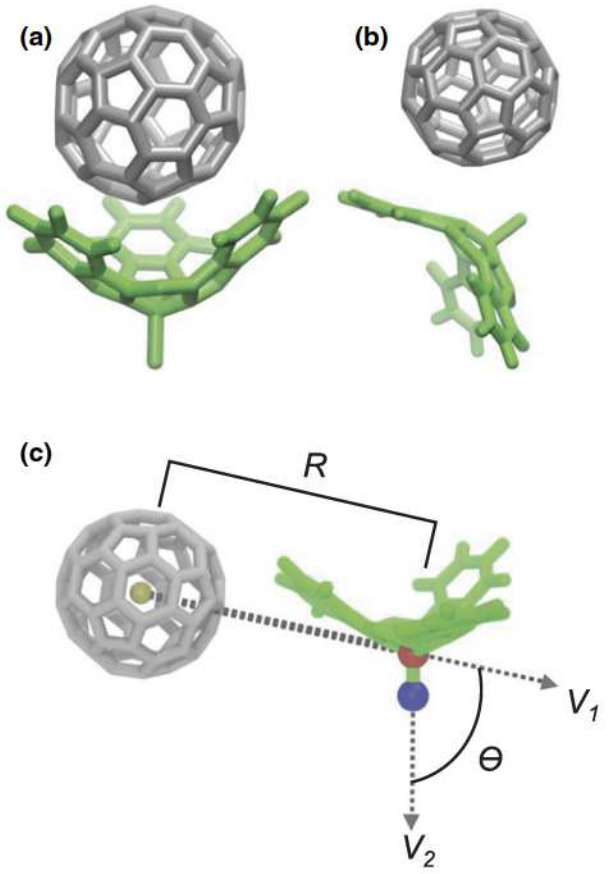

FIG. 1. SubPC (green) / C_{60} (gray) D-A pairs. There are three categories of D-A pair geometries: (a) *on top*, (b) *hollow*, and (c) *edge*. The related order parameters, R and θ, are defined in (c), where the yellow bead corresponds to the center of mass of the C_{60} and the red and blue beads correspond to the boron and chlorine atoms of SubPC, respectively. The R parameter is the distance between the center of mass of C_{60} and the boron atom. The θ parameter is the angle between the two vectors, V_1 and V_2.

We use classical all-atom molecular-dynamics (MD) simulations to obtain an ensemble of interfacial D-A pair geometries. In doing so, we find that the ensemble of geometries is dominated by a third type of a pair geometry, which we refer to as "*edge*" [see Fig. 1(c)], in addition to the *on-top* and *hollow* geometries.

We also investigate how type of geometry, overlooked by earlier gas-phase or PCM calculations, impacts CT rates. To this end, we perform electronic structure calculations on three representative D-A pair geometries and use the results to calculate the distribution of rate constants at the Marcus-theory level (k^M) [25]. The resulting rates are comparable to previously reported experimental and calculated rates [1,18,21]. We also define the corresponding CT rate constant (k^C) as the product of k^M and the charge (ΔQ_D) associated with the CT transition. We find that the amount of charge transferred depends significantly both on the D-A pair geometry and the particular transition involved. While the CT rates are key in determining the cell performance, the rates for other processes involved in the charge separation and collection have to be also determined [17,26].

The fabrication protocol, where the order of the layer deposition is varied, has been shown to impact the device performance and therefore presumably the underlying ensemble of interfacial geometries [5,27]. We address such variant distributions of the interfacial pairs by using extreme cases in setting up the MD simulations and therefore elaborate on the potential impact of the fabrication protocol to enhance the device parameter. For the different cases, MD simulations are analyzed to obtain the statistical weight (p) of each geometry for each model. This allows for measuring the CT rate density (ω^C) for a given model, by summing pk^C for each geometry. Therefore, ω^C allows us to quantify the correlation between interfacial morphology and CT rates. As presented below, we find that maximizing the *on-top* population enhances the performance.

II. RESULTS

A. Interfacial SubPC/C_{60} pair geometries

Classical all-atom MD simulations are performed at 298.15 K within a periodic cubic box containing 75 C_{60} and 75 SubPC molecules for 20 ns. The simulation box is prepared using five protocols to probe the wide range of possible fabrication procedures (see the detailed discussion below in Sec. V and the Supplemental Material [28] for the initial setup of the layers). An ensemble of interfacial D-A

pairs, defined when the closest distance between any atom in C_{60} and any atom in SubPC is no more than 5 Å, is then obtained. The potential of mean force (PMF) is calculated by categorizing the pairs based on two order parameters [see Fig. 1(c)]: (1) R, which is the distance between the center of mass of C_{60} and the boron atom of SubPC; and (2) θ, which is the angle between the vector from the center of mass of C_{60} to the boron atom of SubPC and the vector from the boron atom to the chlorine atom of SubPC [for the PMF of model V, see Fig. 2(a)].

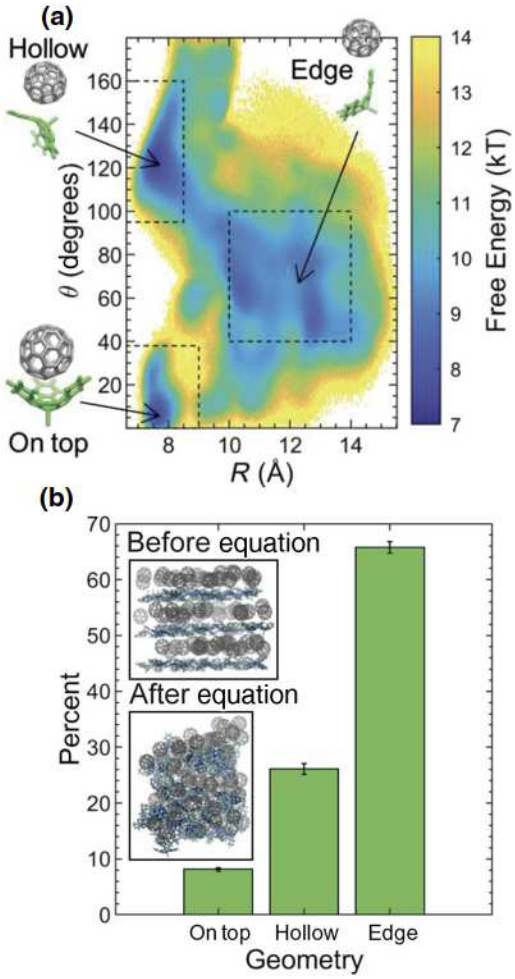

FIG. 2. The potential of mean force (a) and population of pair geometries (b) for the SubPC/C_{60} pair in deposition model V (for the other deposition models introduced below, see Fig. S1 and Sec. I in the Supplemental Material [28]), as a function of the order parameters, R and θ. R and θ are defined in Fig. 1(c). The color is scaled by k_BT. The corresponding ranges of the order parameters for the different spatial pairs are indicated by the rectangular boxes. On top, $R < 8.5$ Å and $\theta < 38°$; hollow, $R < 9$ Å and $95° < \theta < 160°$; edge (the majority), 10 Å $< R <$ 14 Å and $40° < \theta < 100°$. Also shown are representative geometries (*on top*, *hollow*, and *edge*) of SubPC/C_{60} at each of the three major basins. The setup of deposition model V is shown both before and after equilibration as insets in (b).

Inspection of the PMF reveals two pronounced basins centered at $(R,\theta) = (7.5$ Å, $0°)$ and $(R,\theta) = (7.5$ Å, $120°)$, which correspond to the *on-top* [Fig. 1(a)] and *hollow* [Fig. 1(b)] pair geometries, respectively. The corresponding basins on the PMF are defined as $R < 8.5$ Å and $\theta < 38°$ for *on-top* pairs and $R < 9$ Å and $95° < \theta < 160°$ for *hollow* pairs.

We also find a third broad basin on the PMF that does not correspond to either previously identified geometry for interfacial SubPC/C_{60} pairs. This basin consists of pairs where only the *edge* of SubPC is in contact with C_{60}. We refer to this previously overlooked D-A pair geometry as *edge*. The basin for the *edge* geometry corresponds effectively to anything that is not *on top* or *hollow*. The majority of the *edge* pairs fall within the following range: 10 Å $< R <$ 14 Å and $40° < \theta < 100°$. While *edge* geometries have a wide variance in θ, we select one structure as an example to aid visualization, as shown in Figs. 1(c) and 2(a). It should be noted that although the *edge* basin is shallow compared to the *hollow* and/or *on-top* basins, it covers a significantly larger area in the R-θ plane. As a result, the *edge* population is actually larger than that of *on top* or *hollow* [see Fig. 2(b)]. We note that an overwhelming majority of around 90% of all molecules at the interface are involved in more than a single interfacial pair. This, however, does not affect the CT kinetics on the macroscopical scale, which effectively follow the larger rate constants.

B. Electronic structure of SubPC/C_{60} pairs

Three representative D-A pair geometries that correspond to the *on-top*, *hollow*, and *edge* subensembles are selected. Electronic structure calculations are performed on them as described in Sec. V. Figure 3 shows that the low-lying excited states in SubPC/C_{60} pairs involve the highest occupied molecular orbital (HOMO) of SubPC and the lowest unoccupied molecular orbital (LUMO) of either SubPC or C_{60}. More specifically, in all three geometries, the HOMO, HOMO − 1, LUMO+3, and LUMO+4 are localized on SubPC (the donor molecule), while the LUMO, LUMO+1, and LUMO+2 are localized on C_{60} (the acceptor molecule) (see the molecular orbital energies listed in Table S1 in the Supplemental Material [28]). Considering the coupling of the low-lying excitation localized on the donor to a CT state, we find that the HOMO and LUMO+3 localized on the donor are key in the donor state and that the LUMOs of all the pairs localized on the acceptor are key in the CT state (see the highlighted orbitals in Fig. 3).

We next consider the excited state properties by following their energies within the isolated pair (E^{gas}), the oscillator strength (OS), and the charge of the donor molecule (Q_D) (see Fig. 4). States are designated as bright (light absorbing) if they possess significant OS [29] or as dark

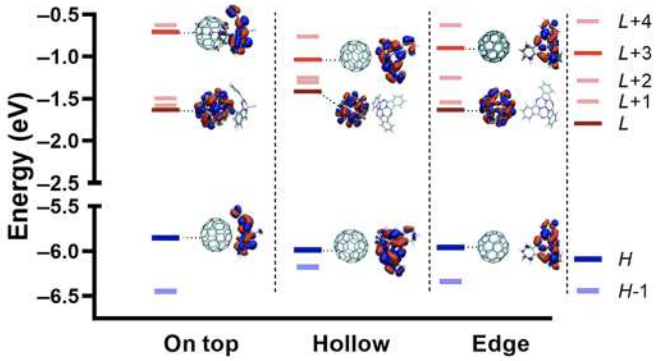

FIG. 3. The orbital energy diagram for the three representative SubPC/C_{60} geometries. The pair's HOMO, shown in blue and denoted as "H," is localized on SubPC. The pair's LUMO, shown in red and denoted as "L," is localized on C_{60} and contributes to all the CT states. The absorbing excited state involves the LUMO on the donor, which is the pair's LUMO+3 shown in red. For the *on-top* geometry, we find an additional absorbing state where the LUMO+4 plays a role (the LUMO+1 on the donor).

if associated with low OS values. Bright absorbing excited states (EX) and CT states also tend to be distinguishable by their Q_D, where the CT states possess $Q_D > 0.10e$. The values of OS and the energies of the main orbitals involved in individual states are listed in Table S2 in the Supplemental Material [28]. States are ordered as $n = 1, 2, 3, \ldots$ according to their ascending gas-phase excitation energy, E^{gas}.

We focus on transitions from bright EX states to dark CT (dCT) states, with one exception: in the *on-top* geometry, we consider a second bright absorbing state that is also a charge-transfer state (bCT), for which both the Q_D and OS are significant. While the EX1 states for the *edge* and *hollow* geometries involve the LUMO on the donor (LUMO+3 of the pair), for the *on-top* geometry, this orbital corresponds to bCT1 and the LUMO+4 is involved in the EX1 state. The detachment and attachment densities of the bCT1 and EX1 states are shown

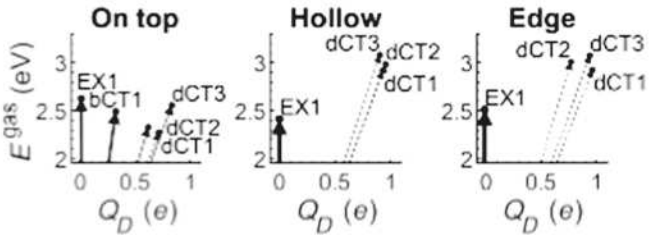

FIG. 4. The charge of the donor molecule (Q_D) in units of e and the excitation energy (E^{gas}) in units of electronvolts for the excited states in different pair geometries. The oscillator strength (OS) is represented by the arrow width. States with a vanishing (< 0.01) OS are represented by a thin dotted line. The numerical values are listed in Table S2 in the Supplemental Material [28].

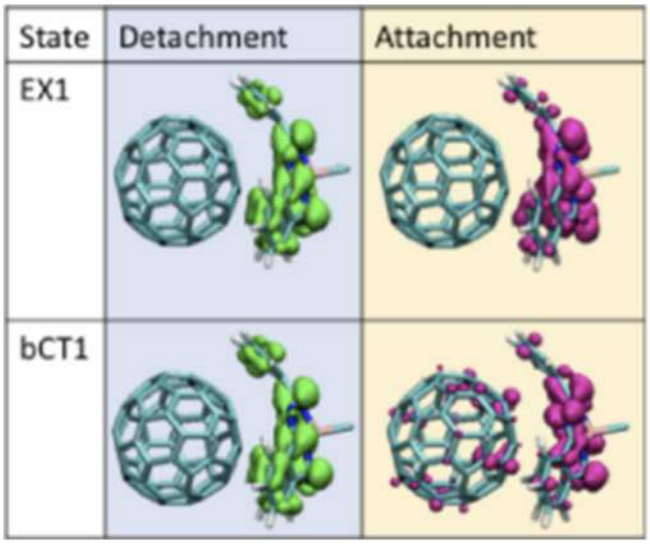

FIG. 5. The detachment (green) and attachment (magenta) electronic densities of the *on-top* EX1 and bCT1 states. Here, the detachment and attachment densities demonstrate that the charge density decreased and increased relative to the corresponding electronic states, respectively. Other excited state densities are shown in Fig. S2 in the Supplemental Material [28].

in Fig. 5 (other detachment and attachment densities are shown in Fig. S2 in the Supplemental Material [28]). For all geometries, we consider several dCT states, the dominant orbital transitions of which are indicated in Table S2 in the Supplemental Material [28].

C. Interfacial charge-transfer rates

We calculate the electronic-population-transfer rate constant, k^M, for transitions from a donor state (EX1 or bCT1) to an acceptor state (dCT1, dCT2, or dCT3) using a Marcus-like expression based on the linearized semiclassical approximation [24,25]. The required inputs to calculate k^M, as shown in Eq. (2) in Sec. V, are a classically sampled D-A energy gap from MD as well as the coupling coefficient, Γ_{DA}, and the excitation-energy correction, W_α, from electronic structure calculations (see Table I and Table S3 in the Supplemental Material [28]). While most studies focus on the rate of transfer from one electronic state to another, k^M, here we introduce a CT rate constant, k^C, to address transitions of varying amounts of charge transferred, ΔQ_D, in the bCT state. The rate constant, k^C, is the product of k^M and ΔQ_D (see Table I). This allows for the evaluation of a transition based on both its rate and the amount of relevant charge. The MD simulations affect the excitation energies by considering the molecular environment. Clearly, the CT states are expected to be more stabilized than the localized excitations [23].

In the *on-top* geometry, the Γ_{DA} for the bCT1 → dCT1 and bCT1 → dCT2 transitions is the largest of all the coupling energies considered by a factor of 2. On the other

TABLE I. The charge-transfer rates (k^C, in amperes) for all three donor-acceptor geometries. For each transition, the electronic coupling between donor and acceptor states (Γ_{DA}, in millielectronvolts), the change in charge of the donor molecule (ΔQ_D, in e), and the mean energy gap ($\langle U \rangle$, in millielectronvolts).

Geometry	Transition	Γ_{DA} (meV)	ΔQ_D (e)	$\langle U \rangle$ (meV)	k^C (A)
	EX1 → dCT1	4.03	0.706	217 ± 2	$1.8(\pm 0.1) \times 10^{-7}$
	EX1 → dCT2	24.46	0.616	148 ± 11	$5.2(\pm 0.7) \times 10^{-7}$
	EX1 → dCT3	5.47	0.825	-168 ± 1	$2.2(\pm 0.1) \times 10^{-7}$
On top	EX1 → bCT1	25.82	0.314	114 ± 5	$5.1(\pm 0.4) \times 10^{-7}$
	bCT1 → dCT1	74.16	0.391	123 ± 2	$2.4(\pm 0.2) \times 10^{-8}$
	bCT1 → dCT2	72.27	0.302	61.6 ± 0.1	$1.01(\pm 0.02) \times 10^{-6}$
	bCT1 → dCT3	21.13	0.511	-240 ± 12	$1.4(\pm 0.8) \times 10^{-11}$
	EX1 → dCT1	1.85	0.943	-743 ± 14	$6(\pm 2) \times 10^{-12}$
Hollow	EX1 → dCT2	21.21	0.959	-837 ± 14	$4(\pm 2) \times 10^{-11}$
	EX1 → dCT3	15.53	0.905	-936 ± 30	$6(\pm 4) \times 10^{-12}$
	EX1 → dCT1	10.30	0.977	-354 ± 23	$6.5(\pm 0.5) \times 10^{-8}$
Edge	EX1 → dCT2	14.02	0.781	-432 ± 15	$3.2(\pm 0.7) \times 10^{-10}$
	EX1 → dCT3	17.22	0.953	-481 ± 20	$3.1(\pm 0.6) \times 10^{-9}$

hand, ΔQ_D for transitions involving bCT1 is smaller than that of other transitions due to the higher Q_D shown in Fig. 4. As a result, the values of k^C for transitions with EX1 and bCT1 as parent states in the *on-top* geometry are comparable (within an order of magnitude) both to each other and to previously calculated values for k^M (however, it should be noted that the states and transitions in the literature do not exactly correspond to those reported here, as the geometries here are taken from MD simulations as opposed to optimized geometries) [1].

For the *hollow* and *edge* geometries, the Γ_{DA} values for transitions from EX1 to dCT states are smaller than for any transitions for the *on top* geometry and consequently are associated with smaller rate constants. Interestingly, the k^C values for the *edge* geometry are faster overall than those of the *hollow* geometry. This is somewhat surprising considering the relatively smaller contact between the donor and acceptor molecules in the *edge* geometry. This difference between *edge* and *hollow* can be traced back to the fact that the transitions in the *edge* geometry correspond to a much smaller $\langle U \rangle$ than those of the *hollow* geometry (see Table I). The k^M values for transitions in the *hollow* geometry (see Table S3 in the Supplemental Material [28]) are observed to be significantly smaller than previously reported [1].

D. Effect of deposition protocols

We consider five deposition models that mimic extreme scenarios of fabrication that are associated with different geometries (see Fig. 6). Models I-III are characterized by an ordered SubPC layer upon which the C_{60} layer is deposited. The ordered SubPC layers in models I and II are arranged such that they are biased toward the *on-top* and *hollow* geometries, respectively. Model III, on the other hand, is unbiased by having alternating layers. Models IV and V are characterized by a disordered SubPC layer deposited on top of an ordered C_{60} layer. The difference between models IV and V is that model V has alternating layers.

We perform MD simulations for these five models and create free-energy surfaces, as shown in Fig. S1 in the Supplemental Material [28]. We then calculate the populations of the three geometries for the five models [see Fig. 7(a)]. We find that for all the deposition models considered, the *edge* geometry is the dominant one. We also find that the relative population of the *on-top* versus the *hollow* geometries depends quite strongly on the deposition model. More specifically, model I (stacked layers—*on top*) leads to the highest *on-top* population, while model II (stacked layers—*hollow*) has the lowest *on-top* population [see Fig. 7(b)]. This is expected, since by design, the SubPC orientations in models I and II favor *on-top* and *hollow* geometries, respectively. Additionally, as expected, the three other models, involving alternating layers and/or random orientations in the SubPC layer, show intermediate relative populations between deposition models I and II.

In addition to different relative populations, each deposition model possesses a different packing density that may impact device performance. Figure 7(c) shows that model II, the interface of which is dominated by pairs in the *hollow* geometry, has the largest number of interfacial pairs per unit area. Model I has an interfacial pair density that, while lower than that of deposition model II, is higher than those of models III-V. Thus, the deposition procedures that are biased toward only one geometry lead to higher packing density.

In Table II, we evaluate the expected device performance based on the deposition model in terms of the CT rate density (ω^C) by considering the populations of

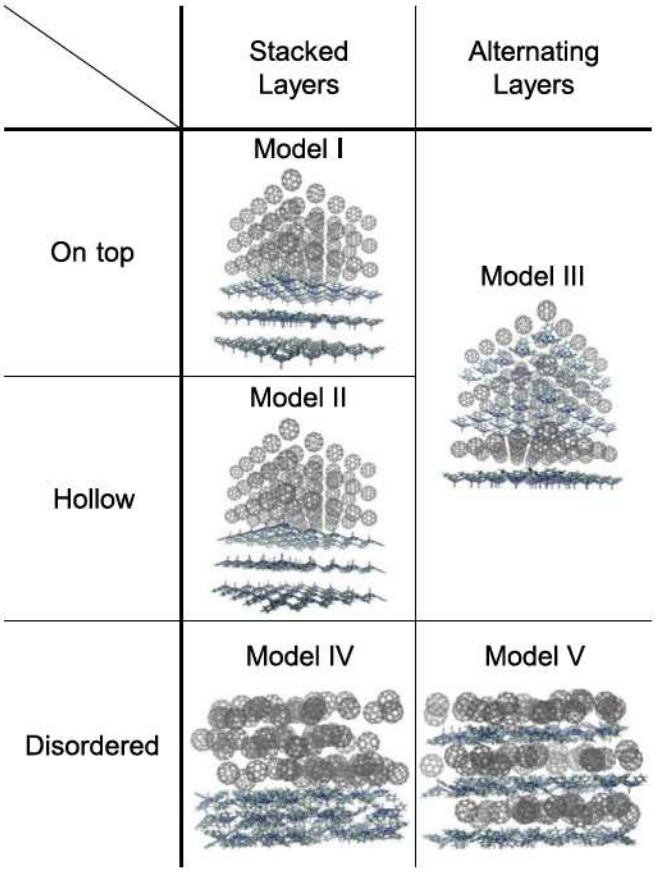

FIG. 6. The five initial conditions mimicking the deposition models used in the simulations. Each consists of six layers of 25 SubPC or C_{60} molecules (three SubPC layers + three C_{60} layers). The models differ with respect to the order of layers and the orientation of the molecules in the SubPC layer. Detailed descriptions can be found in the Supplemental Material [28].

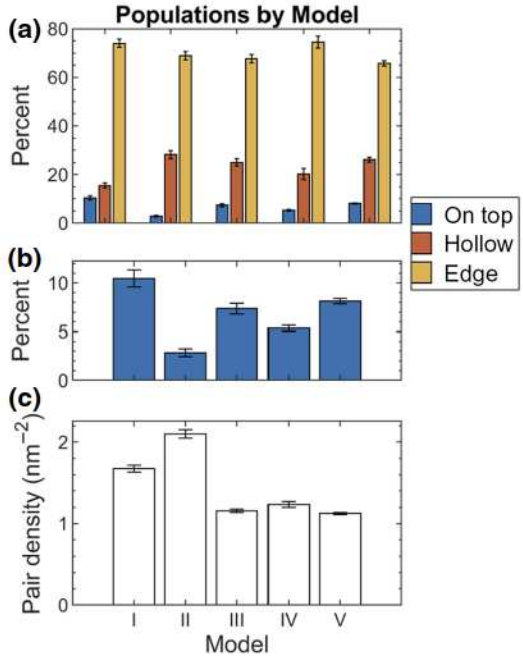

FIG. 7. Interfacial SubPC/C_{60} pairs for the five deposition models in Fig. 6. (a) The percentage of interfacial pairs in the *on-top* (blue), *hollow* (red), and *edge* (yellow) geometries. (b) Only the percentage of interfacial pairs in the *on-top* geometry in each model. (c) The pair density at the interface of each model.

each geometry [Fig. 7(a)], their corresponding k^C values (Table I), and the pair density [Fig. 7(c)]. It should be noted that deposition models I, II, and IV have an interfacial area 5 times smaller than those of models III and V due to their alternating layers. Model I has the largest ω^C value among the five deposition models because it has the largest population of pairs in the *on-top* geometry. The *on-top* geometry dominates ω^C for all deposition models due to its large k^C value, while the *hollow* geometry is nearly insignificant due to its low k^C value. Interestingly, the *edge* geometry plays a significant role because of its large population. As a consequence, all other deposition models give rise to similar performance despite a lower *on-top* population.

III. DISCUSSION

MD simulations are used to obtain an ensemble of interfacial donor-acceptor geometries in the SubPC/C_{60} OPV system. This molecular-level analysis should be contrasted with previous studies that have been based on a dielectric continuum mean-field level of modeling and have yielded only two interfacial geometries (*on top* and *hollow*) [20,21,30,31].

The MD simulations presented in this paper reveal a third interfacial donor-acceptor geometry that we denote by *edge* [see Fig. 1(c)]. The *edge* geometry is not favorable when considered within a continuum dielectric model due to the smaller interfacial overlap between the donor and acceptor molecules. However, the *edge* geometry emerges in the explicit molecular treatment offered by the MD simulations, which reveal that the solid-state environment makes it the dominant geometry in all five deposition models.

We have find that while the k^C value for the *edge* geometry is much lower than that of the *on-top* geometry, the higher population of *edge* still allows it to play a significant

TABLE II. The charge-transfer-rate densities (ω^C in nA/nm^2) for the five deposition models.

ω^C (nA/nm^2)	Model I	Model II	Model III	Model IV	Model V
On top	113 ± 10	39 ± 6	55 ± 4	43 ± 3	59 ± 3
Hollow	0	0	0	0	0
Edge	37 ± 2	43 ± 3	23 ± 2	27 ± 2	22 ± 1
Total	149 ± 11	82 ± 6	78 ± 5	70 ± 4	81 ± 3

role in determining device performance. Such a correlation between interfacial geometry and CT rates is likely not unique for the SubPC/C_{60} system and is expected to play a role in other OPV systems [32–34].

Charge separation in OPV systems follows a sequence of steps that determines the overall efficiency. These steps include charge diffusion [1,2,23,33,35], dissociation [19, 34,36], and recombination [2,35–38], which are associated with a wide range of length and time scales [6,31–35,37, 39–41]. There appears to be evidence that interfacial CT plays a central role in determining the overall device performance and particularly in SubPC/C_{60} systems [5,13,27]. In this study, we focus on the interfacial CT step in a widely studied system, where to better understand the link between structural aspects, including that of the interface and device performance, future work will have to address the other steps and extend the analysis to the mesoscopic level. Essentially, all of the rates of all the steps have to be determined to extract the cell parameters without imposing any assumptions [17,26].

Our simulations address extreme cases of stacked layers. In particular, models I and II of stacked layers increase the occurrence of on-top and hollow interfacial pairs, respectively. See the deposition setups introduced above in Fig. 6. Indeed, while in all cases the edge population is most dominant (between 70% and 80%), in model I we find that over 10% of all pairs are on-top pairs and in model II the on-top fraction drops to 2% and the hollow-pair fraction rises to close to 30%. Consequently, we find that the CT rate density is the largest for model I at 170 nA/nm^2 due to the increased share of the on-top pairs, whereas the other charge densities, including that of model II, are up to around 80 nA/nm^2. This appears to provide a good explanation of the measured trend of the short-circuit current, which is found to be strongly dependent on the order of layer deposition [5]. Further studies are required to directly link the fabrication to the actual distribution of the interfacial pairs affected in the device measurements.

Charge-transfer states are strongly affected by the electrostatic environment, where they can be significantly stabilized to be lower than the absorbing-state energies [42–44]. Therefore, such environmental effects are expected to greatly affect the charge-transfer rates. In this study, we use gas-phase-based electronic structure parameters, where the effects of the environment are captured through the MD simulations. The environmental electrostatic effects stabilize the CT states. We also note that ongoing efforts find that polarization effects addressed by a recently developed polarizable force field yield rates that reproduce the corresponding values achieved using a nonpolarizable force field. While these observations are based on a solvated molecular triad, we also expect to find similar trends, where the polarization terms are only of a secondary effect, when considering OPV-related systems, as in this study. In addition, the recently developed screened range-separated (SRSH) functional [45], which efficiently obtains environment-affected CT states [46], has been used in the study of another OPV fullerene-based system [22] and will be used in the future with MD simulations, as in this study.

IV. CONCLUSIONS

We study the interfacial D-A pairs in SubPC/C_{60} OPV systems, and the associated CT across these pairs. We employ a comprehensive computational framework combining large-scale MD simulations, state-of-the-art quantum chemistry calculations, and the advanced rate theory of photoinduced CT. Large-scale MD simulations are employed to characterize the interfacial D-A pairs.

We find three categories of pairs, including *on-top*, *hollow*, and *edge*. The *edge* conformation, which has not been addressed in previous studies, is found to dominate the interface. However, the *on top* geometry, which comprises a significantly smaller portion of the interface, is found to have comparable CT rates to the *hollow* geometry in studies utilizing a polarizable continuum. The molecular resolution invoked here to study the kinetics identifies it as promoting the CT process most effectively. This interplay of rate constants and conformational density highlights the scope for improving the ability of controlling the fabrication at the molecular level. We predict that increasing the relative weight of *on-top* conformational pairs achieves enhanced CT kinetics across the interface.

V. METHODS

A. Molecular-dynamics simulations

The MD simulations are based on the generalized AMBER force field (GAFF) [47–49]. Interactions involving the Boron atom for SubPC are not provided in GAFF and are therefore adopted from Refs. [50,51] (see Table S4 in the Supplemental Material [28]). In order to examine the effect of fabrication procedures on the interfacial structure, we consider five different sets of initial conditions (see Fig. 6 and detailed descriptions in the Supplemental Material [28]) constructed using a combination of AMBER and PACKMOL [52]:

Model I	Stacked layers(*on top*)
Model II	Stacked layers (*hollow*)
Model III	Alternating layers (on grid)
Model IV	Stacked layers (disordered)
Model V	Alternating layers (disordered)

The MD simulations are performed within AMBER 14 using the program SANDER [47]. Periodic boundary conditions are employed. The initial size of the simulation box varies depending on the initial configurations. The bonds involving hydrogen are constrained using the SHAKE

algorithm [53]. All MD simulations are performed with a time step of 2.0 fs. Electrostatic interactions are computed using the particle-mesh Ewald method [54]. A cutoff of 10 Å is used for van der Waals interactions and real-space Coulomb interactions as well as for updating the neighbor lists.

Energy minimization is performed via a hybrid algorithm. We start out with 500 time steps with the conjugated-gradient method, followed by 4500 time steps with the steepest-descent method. The system is then gradually heated to 298.15 K at constant volume within a 10-ps time interval. This is followed by a 1.0-ns equilibration under an *NPT* ensemble at a constant pressure of 1.0 bar and a temperature of 298.15 K. The pressure relaxation time is set to 1.0 ps. After adjusting the box size to approximately 60 Å × 60 Å × 80 Å based on the equilibrium density, a 20-ns production run under an *NVT* ensemble is performed.

Convergence of the production run is achieved as the Kullback-Leibler (K-L) divergence [55] between distributions of the total potential energy of the system over accumulative simulation time approaches zero at 20 ns (see Fig. S3 in the Supplemental Material [28]). K-L divergence between the probability distribution P (reference) and Q as a function of the order parameter x is defined as follows:

$$\Gamma(P,Q) = -\sum_x P(x)\ln\frac{Q(x)}{P(x)}. \tag{1}$$

The K-L-divergence analysis indicates a well-sampled trajectory if the changes between distributions at different times are small. A value of zero indicates that the two distributions are identical. We systematically calculate the K-L divergence between the distributions of accumulated trajectories at a simulation time interval of 1 ns. The results of our analysis indicate that simulations for all deposition models have reached convergence since the K-L divergence between potential energy distributions approaches zero by the end of our simulation runs.

For further analysis, interfacial donor-acceptor pairs are defined when the closest distance between any atom in C_{60} and any atom in SubPC is no more than 5 Å.

B. Electronic structure calculations

All electronic structure calculations are performed using Q-Chem 4 [56]. Excited-state electronic structure calculations are performed via time-dependent density-functional theory (TD-DFT) on the selected donor-acceptor pairs [57]. The Baer-Neuhauser-Livshits (BNL) range-separated hybrid functional [58,59] and the 6-31G* basis set [60] are used. An optimally tuned γ of 0.167 bohr^{-1}, obtained based on the J2(γ) scheme [61] for the *on-top* geometry, is used in all of the calculations. The electronic coupling coefficients between the donor and acceptor electronic states are calculated via the fragment-charge-differences (FCD) method [62].

Electronic excited states are classified based on the charge of the donor molecule, Q_D, either as non-CT states ($Q_D < 0.10\ e$) or CT states ($Q_D > 0.10\ e$). The non-CT states and CT states are denoted as EXn and CTn, respectively. The index n is used to order the states within a class by their energy, from lowest to highest. CT states with a significant oscillator strength (OS) are referred to as light-absorbing or *bright* (bCT), whereas CT states with negligible OS are referred to as *dark* (dCT).

C. Rate constants

Electronic-population-transfer rate constants are calculated based on the Marcus-like theory outlined in Ref. [25]:

$$k^M = \frac{|\Gamma_{DA}|^2}{\hbar}\sqrt{\frac{2\pi}{\sigma_U^2}}\exp\left[-\frac{\langle U\rangle^2}{2\sigma_U^2}\right]. \tag{2}$$

Here, $U(\mathbf{R}) = V_D(\mathbf{R}) - V_A(\mathbf{R})$ is the donor-acceptor energy gap as a function of the nuclear configuration, $\mathbf{R}$, where V_D and V_A refer to the potential-energy surfaces that correspond to the donor and acceptor states, respectively. $\langle U\rangle$ is the average donor-acceptor energy gap sampled classically on the equilibrated donor state and $\sigma_U = \sqrt{\langle U^2\rangle - \langle U\rangle^2}$ is the corresponding standard deviation. The reorganization energy, E_r, the reaction free energy, ΔE, and the activation energy, E_A, can be expressed in terms of $\langle U\rangle$ and σ_U: $E_r = \sigma_U^2/(2k_BT)$, $\Delta E = -E_r - \langle U\rangle$, and $E_A = k_BT\langle U\rangle^2/(2\sigma_U^2)$. These are listed in Table S5 in the Supplemental Material [28] for each transition. Importantly, using classical MD simulations to calculate U accounts for the environmental effects of explicit ground-state condensed-phase SubPC and C_{60} molecules on the charge-transfer SubPC/C_{60} pair, the electronic excitation energies of which are obtained from electronic structure calculations as detailed in Sec. V.B.

$\langle U\rangle$ and σ_U for a given transition are calculated from *NVT* MD simulations. In these simulations, a SubPC/C_{60} pair is designated and kept fixed. These fixed atoms are assigned with force-field parameters (Mulliken partial charges) of a donor state using the electronic structure approach for the pair. The rest of the SubPC and C_{60} molecules move freely and are assigned the force-field parameters of the ground state. Using the coordinates and velocities of a completed trajectory, V_D^M and V_A^M are found by recalculating the energy of the entire system using MD, as denoted by M. To address double counting between the electronic structure and MD calculations, we define $V_\alpha = V_\alpha^M + W_\alpha$, where W_α is the energy correction and α denotes a donor or acceptor state. W_α is computed as the difference of the single-point energy for each state of the SubPC/C_{60} pair between quantum chemistry calculations and MD simulations in Table S6 in the Supplemental

Material [28]. For each D-to-A transition, U is calculated by finding the difference of V_D and V_A at each time step of 1 ps. Then, $\langle U \rangle$ is obtained by averaging over 40 MD trajectories (40 ns each).

As shown in Fig. S4 in the Supplemental Material [28], the distribution of $U(\mathbf{R})$ is not Gaussian. This is attributed to different solid-state environments that correspond to different local minima. Contributions from different solid-state environments are resolved by best fitting the distribution of $U(\mathbf{R})$ to a sum of Gaussian distributions. The distributions are chosen by least-squares fitting, with the number of Gaussian distributions chosen to be three unless the confidence intervals of the standard deviation contain negative numbers. If not, it is decreased until that criterion is satisfied. These parameters are listed in Table S3 in the Supplemental Material [28]. Investigation of the physical nature of the solid-state environment underlying the different Gaussian distributions is currently under way and will be reported in a separate future publication.

While previous papers have focused on k^M, in this paper we focus on k^C, which incorporates the amount of charge transferred in the transition, ΔQ_D, in order to be a CT rate constant. It is defined as follows:

$$k^C = \Delta Q_D k^M. \tag{3}$$

D. Charge-transfer-rate densities

To estimate the overall CT performance of a certain interfacial morphology, we first define the CT rate constant for a geometry k_i^C ($i \in \{on\ top, hollow, edge\}$) as the sum of the k^C values of all possible D-to-A transitions (t):

$$k_i^C = \sum_t k_t^C, \tag{4}$$

where the k_t^C values for each transition are given in Table I. The CT-rate density ω^C for each deposition model is the weighted CT rate constant for all geometries across a unit area of interface:

$$\omega^C = \sum_i k_i^C p_i \times \frac{\text{number of interfacial pairs}}{\text{area of interface}}, \tag{5}$$

where p is the fraction of a specific geometry.

ACKNOWLEDGMENTS

We are grateful to the Department of Energy (Grant No. DE-SC0016501) and the National Science Foundation (NSF) (Grants No. PHY-1427654 and No. CHE-1362504) for their support. This project utilized the computational resources from the National Energy Research Scientific Computing Center (NERSC), a U.S. Department of Energy Office of Science User Facility operated under Contract No. DE-AC02-05CH11231, the uHPC cluster managed by the University of Houston and acquired through NSF Award No. OAC 1531814, as well as the Ohio Supercomputer Center (OSC) [63] and the Kent State University, College of Arts and Sciences Computing Cluster. X.S. acknowledges support from the National Natural Science Foundation of China (No. 21903054).

[1] M. H. Lee, E. Geva, and B. D. Dunietz, Calculation from first-principles of golden rule rate constants for photoinduced subphthalocyanine/fullerene interfacial charge transfer and recombination in organic photovoltaic cells, J. Phys. Chem. C **118**, 9780 (2014).

[2] Y. Zhao and W. Liang, Charge transfer in organic molecules for solar cells: Theoretical perspective, Chem. Soc. Rev. **41**, 1075 (2012).

[3] J. Kim and S. Yim, Influence of surface morphology evolution of SubPC layers on the performance of SubPC/C_60 organic photovoltaic cells, Appl. Phys. Lett. **99**, 193303 (2011).

[4] H. Tian, Z. Yu, A. Hagfeldt, L. Kloo, and L. Sun, Organic redox couples and organic counter electrode for efficient organic dye-sensitized solar cells, J. Am. Chem. Soc. **133**, 9413 (2011).

[5] X. Tong, B. E. Lassiter, and S. R. Forrest, Inverted organic photovoltaic cells with high open-circuit voltage, Org. Electron. **11**, 705 (2010).

[6] A. Hagfeldt, G. Boschloo, L. Sun, L. Kloo, and H. Pettersson, Dye-sensitized solar cells, Chem. Rev. **110**, 6595 (2010).

[7] M. H. Lee, B. D. Dunietz, and E. Geva, Donor-to-donor vs donor-to-acceptor interfacial charge transfer states in the phthalocyanine-fullerene organic photovoltaic system, J. Phys. Chem. Lett. **5**, 3810 (2014).

[8] D. Balamurugan, A. J. A. Aquino, F. de Dios, L. Flores Jr, H. Lischka, and M. S. Cheung, Multiscale simulation of the ground and photo-induced charge-separated states of a molecular triad in polar organic solvent: Exploring the conformations, fluctuations, and free energy landscapes, J. Phys. Chem. B **117**, 12065 (2013).

[9] V. D'innocenzo, G. Grancini, M. J. P. Alcocer, A. R. S. Kandada, S. D. Stranks, M. M. Lee, G. Lanzani, H. J. Snaith, and A. Petrozza, Excitons versus free charges in organo-lead tri-halide perovskites, Nat. Commun. **5**, 3586 (2014).

[10] J.-L. Brédas, D. Beljonne, V. Coropceanu, and J. Cornil, Charge-transfer and energy-transfer processes in π-conjugated oligomers and polymers: A molecular picture, Chem. Rev. **104**, 4971 (2004).

[11] C. W. Tang and S. A. VanSlyke, Organic electroluminescent diodes, Appl. Phys. Lett. **51**, 913 (1987).

[12] K. L. Mutolo, E. I. Mayo, B. P. Rand, S. R. Forrest, and M. E. Thompson, Enhanced open-circuit voltage in subphthalocyanine/C_{60} organic photovoltaic cells, J. Am. Chem. Soc. **128**, 8108 (2006).

[13] N. Ilyas, S. S. Harivyasi, P. Zahl, R. Cortes, O. T Hofmann, P. Sutter, E. Zojer, and O. L. A. Monti, Sticking with the pointy end? Molecular configuration of chloro

boron-subphthalocyanine on Cu(111), J. Phys. Chem. C **120**, 7113 (2016).
[14] G. D'Avino, L. Muccioli, F. Castet, C. Poelking, D. Andrienko, Z. G. Soos, J. Cornil, and D. Beljonne, Electrostatic phenomena in organic semiconductors: Fundamentals and implications for photovoltaics, J. Phys. Condens. Matter **28**, 433002 (2016).
[15] D. S. Josey, S. R. Nyikos, R. K. Garner, A. Dovijarski, J. S. Castrucci, J. M. Wang, G. J. Evans, and T. P. Bender, Outdoor performance and stability of boron subphthalocyanines applied as electron acceptors in fullerene-free organic photovoltaics, ACS Energy Lett. **2**, 726 (2017).
[16] R. Pandey, A. A. Gunawan, K. A. Mkhoyan, and R. J. Holmes, Efficient organic photovoltaic cells based on nanocrystalline mixtures of boron subphthalocyanine chloride and C_{60}, Adv. Func. Mater. **22**, 617 (2012).
[17] N. C. Giebink, B. E. Lassiter, G. P. Wiederrecht, M. R. Wasielewski, and S. R. Forrest, Ideal diode equation for organic heterojunctions. II. the role of polaron pair recombination, Phys. Rev. B **82**, 155306 (2010).
[18] Daniel E. Wilcox, Myeong H. Lee, Matthew E. Sykes, Andrew Niedringhaus, Eitan Geva, Barry D. Dunietz, Max Shtein, and Jennifer P. Ogilvie, Ultrafast charge-transfer dynamics at the boron subphthalocyanine chloride/C_{60} heterojunction: Comparison between experiment and theory, J. Phys. Chem. Lett. **6**, 569 (2015).
[19] Y. Yi, V. Coropceanu, and J.-L. Brédas, Exciton-dissociation and charge-recombination processes in pentacene/C_{60} solar cells: Theoretical insight into the impact of interface geometry, J. Am. Chem. Soc. **131**, 15777 (2009).
[20] S. E. Morris, Ph.D. thesis, College of Engineering, University of Michigan, 2014.
[21] M. H. Lee, E. Geva, and B. D. Dunietz, The effect of interfacial geometry on charge-transfer states in the phthalocyanine/fullerene organic photovoltaic system, J. Phys. Chem. A **120**, 2970 (2016).
[22] Y. Song, A. Schubert, X. Liu, S. Bhandari, S. R. Forrest, B. D. Dunietz, E. Geva, and J. P. Ogilvie, Efficient charge generation via hole transfer in dilute organic donor–fullerene blends, J. Phys. Chem. Lett. **11**, 2203 (2020).
[23] A. K. Manna, D. Balamurugan, M. S. Cheung, and B. D. Dunietz, Unraveling the mechanism of photoinduced charge transfer in carotenoid-porphyrin-C_{60} molecular triad, J. Phys. Chem. Lett. **6**, 1231 (2015).
[24] X. Sun, P. Zhang, Y. Lai, K. L. Williams, M. S. Cheung, B. D. Dunietz, and E. Geva, Computational study of charge-transfer dynamics in the carotenoid-porphyrin-C_{60} molecular triad solvated in explicit tetrahydrofuran and its spectroscopic signature, J. Phys. Chem. C **122**, 11288 (2018).
[25] X. Sun and E. Geva, Equilibrium Fermi's golden rule charge transfer rate constants in the condensed phase: The linearized semiclassical method vs. classical Marcus theory, J. Phys. Chem. A **120**, 2976 (2016).
[26] N. C. Giebink, G. P. Wiederrecht, M. R. Wasielewski, and S. R. Forrest, Thermodynamic efficiency limit of excitonic solar cells, Phys. Rev. B **83**, 195326 (2011).
[27] C. Stadler, S. Hansen, I. Kröger, C. Kumpf, and E. Umbach, Tuning intermolecular interaction in long-range-ordered submonolayer organic films, Nat. Phys. **5**, 153 (2009).
[28] See the Supplemental Material at http://link.aps.org/supplemental/10.1103/PhysRevApplied.13.054075 for details of the setup for the MD simulations, the electronic excitation properties, densities, and orbital energies, the probability density for the EX1-to-CT1 transition of *hollow*, transfer rates and semiclassical parameters, and force-field parameters.
[29] James W. Robinson, *Atomic Spectroscopy* (CRC Press, 1996).
[30] S. E. Morris, D. Bilby, M. E. Sykes, H Hashemi, M. J. Waters, J. Kieffer, J. Kim, and M. Shtein, Effect of axial halogen substitution on the performance of subphthalocyanine based organic photovoltaic cells, Org. Electron. **15**, 3660 (2014).
[31] M. Xiao, Y. Tian, and S. Zheng, An insight into the relationship between morphology and open circuit voltage/electronic absorption spectrum at donor-acceptor interface in boron subphthalocyanine chloride/C_70 solar cell: A DFT/TDDFT exploration, Org. Electron. **59**, 279 (2018).
[32] N. E. Jackson, B. M. Savoie, T. J. Marks, L. X. Chen, and M. A. Ratner, The next breakthrough for organic photovoltaics?, J. Phys. Chem. Lett. **6**, 77 (2015).
[33] M. L. Jones and E. Jankowski, Computationally connecting organic photovoltaic performance to atomistic arrangements and bulk morphology, Mol. Simul. **43**, 756 (2017).
[34] H. M. Heitzer, B. M. Savoie, T. J. Marks, and M. A. Ratner, Organic photovoltaics: Elucidating the ultra-fast exciton dissociation mechanism in disordered materials, Angew. Chem. Int. Ed. Engl. **53**, 7456 (2014).
[35] J. Kurpiers, T. Ferron, S. Roland, M. Jakoby, T. Thiede, F. Jaiser, S. Albrecht, S. Janietz, B. A. Collins, I. A. Howard *et al.*, Probing the pathways of free charge generation in organic bulk heterojunction solar cells, Nat. Commun. **9**, 2038 (2018).
[36] M. Causa', J. De Jonghe-Risse, M. Scarongella, J. C. Brauer, E. Buchaca-Domingo, J.-E. Moser, N. Stingelin, and N. Banerji, The fate of electron-hole pairs in polymer: Fullerene blends for organic photovoltaics, Nat. Commun. **7**, 12556 (2016).
[37] J. Teuscher, J. C. Brauer, A. Stepanov, A. Solano, A. Boziki, M. Chergui, J.-P. Wolf, U. Rothlisberger, N. Banerji, and J.-E. Moser, Charge separation and carrier dynamics in donor-acceptor heterojunction photovoltaic systems, Struct. Dyn. **4**, 061503 (2017).
[38] J.-L. Brédas, J. E. Norton, J. Cornil, and V. Coropceanu, Molecular understanding of organic solar cells: The challenges, Acc. Chem. Res. **42**, 1691 (2009).
[39] G. J. Hedley, A. J. Ward, A. Alekseev, C. T. Howells, E. R. Martins, L. A. Serrano, G. Cooke, A. Ruseckas, and Ifor D. W. Samuel, Determining the optimum morphology in high-performance polymer-fullerene organic photovoltaic cells, Nat. Commun. **4**, 2867 (2013).
[40] Y. Liu, J. Zhao, Z. Li, C. Mu, W. Ma H. Hu, K. Jiang, H. Lin, H. Ade, and H. Yan, Aggregation and morphology control enables multiple cases of high-efficiency polymer solar cells, Nat. Commun. **5**, 5293 (2014).
[41] P. Docampo, J. M. Ball, M. Darwich, G. E. Eperon, and H. J. Snaith, Efficient organometal trihalide perovskite planar-heterojunction solar cells on flexible polymer substrates, Nat. Commun. **4**, 2761 (2013).

[42] S. Zheng, H. Phillips, E. Geva, and B. D. Dunietz, *Ab initio* study of the emissive charge-transfer states of solvated chromophore-functionalized silsesquioxanes, J. Am. Chem. Soc. **134**, 6944 (2012).

[43] H. Phillips, E. Geva, and B. D. Dunietz, Calculating off-site excitations in symmetric donor-acceptor systems via time-dependent density functional theory with range-separated density functionals, J. Chem. Theory Comput. **8**, 2661 (2012).

[44] H. Phillips, Z. Zheng, E. Geva, and B. D. Dunietz, Orbital gap predictions for rational design of organic photovoltaic materials, Org. Electron. **15**, 1509 (2014).

[45] S. Bhandari, M. Cheung, E. Geva, L. Kronik, and B. D. Dunietz, Fundamental gaps of condensed-phase organic semiconductors from single-molecule polarization-consistent optimally tuned screened range-separated hybrid functionals, J. Chem. Theory Comput. **14**, 6287 (2018).

[46] S. Bhandari and B. D. Dunietz, Quantitative accuracy in calculating charge transfer state energies in solvated molecular dimers using screened range separated hybrid functional within a polarized continuum model, J. Chem. Theory Comput. **15**, 4305 (2019).

[47] D. A. Case, V. Babin, J. Berryman, R. M. Betz, Q. Cai, D. S. Cerutti, T. E. Cheatham Iii, T. A. Darden, R. E. Duke, H. Gohlke *et al.*, AMBER 14, University of California, 2014.

[48] J. M. Wang, W. Wang, P. A. Kollman, and D. A. Case, Automatic atom type and bond type perception in molecular mechanical calculations, J. Mol. Graph. **25**, 247 (2006).

[49] J. M. Wang, R. M. Wolf, J. W. Caldwell, P. A. Kollman, and D. A. Case, Development and testing of a general AMBER force field, J. Comput. Chem. **25**, 1157 (2004).

[50] C. G. Claessens, D. Gonzalez-Rodriguez, and T. Torres, Subphthalocyanines: Singular nonplanar aromatic compounds synthesis, reactivity, and physical properties, Chem. Rev. **102**, 835 (2002).

[51] X. Wu, Z. Liu, S. Huang, and W. Wang, Molecular dynamics simulation of room-temperature ionic liquid mixture of [bmim][BF_4] and acetonitrile by a refined force field, Phys. Chem. Chem. Phys. **7**, 2771 (2005).

[52] L. Martinez, R. Andrade, E. G. Birgin, and J. M. Martinez, PACKMOL: A package for building initial configurations for molecular dynamics simulations, J. Comput. Chem. **30**, 2157 (2009).

[53] G. Ciccotti and J.-P. Ryckaert, Molecular dynamics simulation of rigid molecules, Comput. Phys. Rep. **4**, 346 (1986).

[54] T. Darden, D. York, and L. Pedersen, The effect of long-range electrostatic interactions in simulations of macromolecular crystals—A comparison of the Ewald and truncated list methods, J. Chem. Phys **98**, 10089 (1993).

[55] S. Kullback and R. A. Leibler, On information and sufficiency, Ann. Math. Stat. **22**, 79 (1951).

[56] Y. Shao *et al.*, Advances in methods and algorithms in a modern quantum chemistry program package, Phys. Chem. Chem. Phys. **8**, 3172 (2006).

[57] E. Runge and E. K. U. Gross, Density-Functional Theory for Time-Dependent Systems, Phys. Rev. Lett. **52**, 997 (1984).

[58] R. Baer and D. Neuhauser, Density Functional Theory with Correct Long-Range Asymptotic Behavior, Phys. Rev. Lett. **94**, 043002 (2005).

[59] E. Livshits and R. Baer, A well-tempered density functional theory of electrons in molecules, Phys. Chem. Chem. Phys. **9**, 2932 (2007).

[60] V. A. Rassolov, J. A. Pople, M. A. Ratner, and T. L. Windus, 6-31G* basis set for atoms K through Zn, J. Chem. Phys. **109**, 1223 (1998).

[61] T. Stein, L. Kronik, and R. Baer, Prediction of charge-transfer excitations in coumarin-based dyes using a range-separated functional tuned from first principles, J. Chem. Phys. **131**, 244119 (2009).

[62] A. A. Voityuk and N. Rösch, Fragment charge difference method for estimating donor-acceptor electronic coupling: Application to DNA π-stacks, J. Chem. Phys. **117**, 5607 (2002).

[63] Ohio Supercomputer Center, http://osc.edu/ark:/19495/f5s1ph73.